LOCAL TEMPERATURE DISTRIBUTION OF A PLATE HEAT EXCHANGER UNDERGOING CRYSTALLIZATION FOULING

*J. Berce, M. Može, M. Zupančič and I. Golobič
University of Ljubljana, Faculty of Mechanical Engineering,
Aškerčeva cesta 6, SI-1000 Ljubljana, Slovenia
*jure.berce@fs.uni-lj.si

ABSTRACT

The compact design of plate heat exchangers prevents local insights during system operation, which would be desired when designing for and evaluating a given fouling problem. Severe foulant build-up is often confined to specific regions within the flow channel geometry and could be mitigated to an extent by managing the distribution of flow if areas with high susceptibility towards fouling could be identified.

We conducted laboratory crystallization fouling experiments on a counter-current brazed plate heat exchanger, coupling real-time measurements of flow rates and temperatures with infrared thermography. This non-intrusive method of spatiotemporal plate temperature characterization allowed local detection and evaluation of severely fouled areas within the upper channel. In the investigated case, the highest susceptibility towards salt crystallization was observed in the flow stagnation zone near the hot outlet, where the largest temperature gradient between both fluids was present and the driving supersaturation was largest. Apart from its use in future plate heat exchanger design, the presented approach can be coupled with computational fluid dynamics simulations, as was illustrated in this work.

INTRODUCTION

Among the distinct fouling mechanisms, crystallization represents the most severe influence in practical use of many heat exchangers, notably reducing thermal performance and increasing pressure drop across the unit [1]. Scaling occurs when the solution becomes supersaturated, which in thermal systems most often occurs due to changes in temperature that in turn affects the solubility of a given substance. Sparingly soluble salts, such as calcium carbonate or sulphate, exhibit an inverse temperature dependance of solubility, therefore depositing on heated surfaces. The fouling process itself is governed by the concentration driving force, inducing deposition, as well as the wall shear stress that causes deposit removal. Therefore, to mitigate and manage a scaling problem within a plate type heat exchanger (PHE), favorable flow distribution between plates is sought, which requires one to consider the implications of fouling in the design process. Nowadays, this is often achieved with the help of computational fluid dynamics (CFD), whose results are highly dependent on user-settings and limited by system size in connection to computational demand. On the other hand, local non-invasive experimental insight into fouling of a plate heat exchanger remains elusive, with only a few studies available that have bridged the gap, most often by adapting the studied heat exchanger geometry to some extent. Kho et al. [2] conducted fouling experiments in a plate heat exchanger where the upper plate was replaced with a transparent flat polycarbonate replica. ABS particles were added to water, and their deposition inside the channel could be observed in real time with a video camera. The authors later extended this approach to study calcium sulphate fouling between flat stainless-steel plates with different flow distributors [3]. To prevent the occurrence of deposits in flow stagnation areas the distributor design was varied. However, in the wake of these distributors, new low flow velocity zones were created, which could even increase the overall fouling in the unit. With the advancement of more complicated plate corrugation patterns, like the dimple pattern, or even in case of traditional chevron-type patterns, the simplifications of channel geometry which allow local insight might not be representative of fouling that one might expect when operating the unit in practice. We aim to avoid these drawbacks of flow channel geometry modifications by using infrared (IR) thermography to study the spatiotemporal plate temperature during fouling. In the past, similar approaches were successfully applied to various studies of PHE operation. Freund and Kabelac [4] obtained a map of local convective heat transfer coefficients, based on temperature oscillations of the heat–transferring wall determined by an infrared camera. Sarraf et al. [5], when studying pentane condensation in a plate heat exchanger, used the acquired temperature map to determine vapor quality, condensation heat transfer coefficient and heat flux. Amalfi and Thome [6,7] studied the single-phase flow of refrigerants in a channel of a compact PHE, heated by electrical

current. Infrared thermography was coupled with conventional temperature and flow rate and pressure drop sensors to obtain local and integral heat transfer data. Several flow regimes were tested, and locations of flow maldistribution was identified.

The promising results of aforementioned past studies led us to extend this non-intrusive technique to the study of BPHE fouling, where the use of IR thermography is surprisingly limited at the moment. The spatiotemporal changes of temperature, induced by fouling, are important when analysing a HE performance and lifespan. Aside from the removal of one end plate, our approach requires no changes to the plate heat exchanger, meaning that any observation can be directly applicable to practical operation. It can serve as a foundation for future research of heat exchanger operation in the presence of fouling, for verification of computational models or for research and development of new plate patterns.

MATERIALS AND METHODS

Experiments were conducted on a brazed plate heat exchanger (BPHE) with a sinusoidal dimple plate pattern without the thicker upper end plate. The unit with four stainless-steel plates (composing three flow channels), operating in a counter–current flow configuration, was installed in an experimental setup schematically shown in Figure 1. Hot deionized (DI) water was circulated through the middle channel, while the outer two channels were transporting an artificially prepared calcium carbonate salt solution (i.e., synthetic hard water), which was the source of crystallization fouling within the unit. The solution was prepared at room temperature by dissolving calcium nitrate tetrahydrate and sodium bicarbonate into separate reservoirs of DI water. Both aqueous solutions were then homogeneously mixed, yielding an equilibrated supersaturated calcium carbonate solution with a concentration of 0,98 g/L and a pH of 7,4. During experiments, inlet and outlet temperatures, volumetric flow rates and the pressure drop in the cold section were monitored and recorded every second. Additionally, infrared videos were recorded at constant time intervals with the camera, which was positioned 0.5 m away from the

BPHE, yielding a spatial resolution of 0,472 mm/pixel. The outward-facing area of the upper plate was spray–coated with high emissivity paint, minimizing the reflection from ambient surfaces while increasing the detected emitted radiation. Due to its high thermal conductivity (78 W m^{-1} K^{-1}), low thickness (3 – 5 μm) and expected low heat transfer coefficient to the outside stationary air, the additional thermal resistance of the paint was assumed negligibly small. Additionally, the surface radiative properties (ε = 0,92) of the paint were independent of substrate material when the coating thickness exceeded 2 microns.

The infrared camera was factory calibrated within the temperature range of – 40 °C to 150 °C at a known surface emissivity. Its measurement uncertainty contributions include the determination of emissivity, the distance to the object, ambient reflections, and the attenuation of infrared radiation. The standard measurement uncertainty of measured plate surface temperature, fluid temperatures and volumetric flow rates is given by Table 1.

Table 1. Standard measurement uncertainty of measured quantities within this study.

Quantity	Sensor	Uncertainty
Fluid temperature	K- type thermocouple	± 1,5°C
Volumetric flow rate	Electromagnetic flowmeter	± 1% of reading
Plate surface temperature	Infrared camera	± 2°C

The thin plates, made of 0,25 mm AISI 316L stainless steel, enclosing narrow flow channels (1,5 – 3 mm height) which facilitate fluid mixing, allowed the assumption that the measured temperature of the upper thin plate is indicative of the cold solution temperature flowing underneath. This was validated by comparing the inlet and outlet temperatures measured by K-type thermocouples and the values at the corresponding sections of the IR images. During all experiments, the temperature trends were clearly detected by the camera, and the
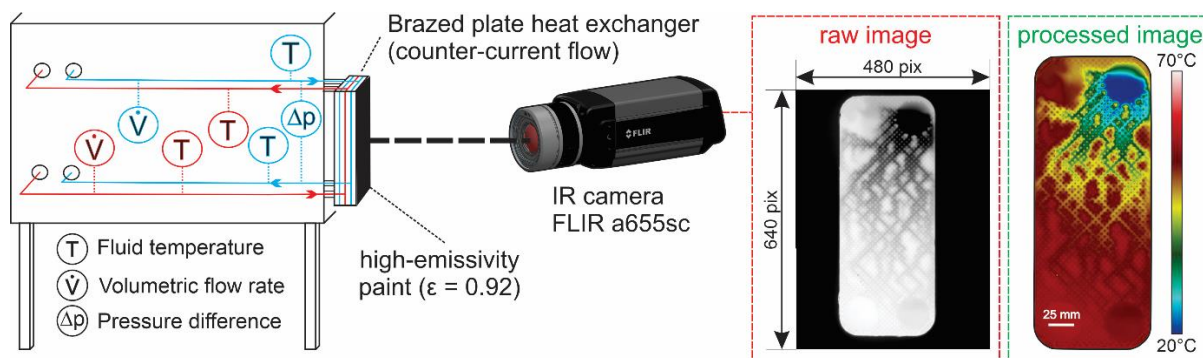

Figure 1. Experimental setup for measuring outer plate temperature distribution, fluid inlet and outlet temperatures, volumetric flow rates and pressure difference.

discrepancy between both measurements was within 3% in the whole temperature range.

Each experimental run was initialized with DI water to achieve temperature equilibrium in the setup. After the temperatures stabilized, the salt solution was released through the cold section and the measurements were started. From measured flow rates and temperatures one can obtain the real time performance of a single pass counter-current heat exchanger in the form of an overall heat transfer coefficient [8]:

$$U = \dot{Q}/(A \cdot LMTD) \qquad (1)$$

Here, A is the known heat exchange area, $\dot{Q}$ the heat flow rate and $LMTD$ the mean logarithmic temperature difference between the two fluid streams. To offset heat losses (less than 0.4% in the later-presented data), the exchanged heat flow rate can be calculated as an average of both fluid streams:

$$\dot{Q} = (\dot{Q}_h + \dot{Q}_c)/2 \qquad (2)$$

$$\dot{Q}_h = \dot{m}_h \cdot c_{p,h} \cdot (T_{h,in} - T_{h,out}) \qquad (3)$$

$$\dot{Q}_c = \dot{m}_c \cdot c_{p,c} \cdot (T_{c,out} - T_{c,in}) \qquad (4)$$

While the logarithmic mean temperature difference is obtained from measured inlet and outlet temperature values:

$$LMTD = \frac{(T_{h,in} - T_{c,out}) - (T_{h,out} - T_{c,in})}{\ln((T_{h,in} - T_{c,out})/(T_{h,out} - T_{c,in}))} \qquad (5)$$

With the progression of fouling, the heat flow rate between fluid streams decreases, the mean temperature difference increases and as a result, the overall heat transfer coefficient decreases. To characterize this performance degradation at a given point in time, the current (at a time instance t) overall heat transfer coefficient U_t can be compared to its value in clean (or initial) conditions U_0 to obtain the added thermal resistance induced by the deposit:

$$R_f = 1/U_t - 1/U_0 \qquad (6)$$

This variable, called fouling resistance, features the deposit-induced changes to conductive as well as convective thermal resistance on one or both sides of the fluid separating wall, and is increasing with the progression of fouling. Depending on process conditions and the fouling mechanisms that appear, the R_f curve manifests distinctly different shape. Linear and falling rate curves are rare in long experimental durations, and the most commonly recorded shape is the asymptotic one. Saw-tooth oscillations of various intensity are also common, due to substantial deposit break-off [9].

RESULTS AND DISCUSSION

The fouling experiment in the BPHE was left running for 410 minutes with constant flow rates and inlet temperatures, yielding a repeatable fouling resistance value of $3{,}2 \cdot 10^{-4}$ m^2 K W^{-1} (Figure 2). To induce a high temperature increase and fast crystallization, the flow rate of the cold solution was intentionally set to low values ($v = 0{,}08$ m s^{-1}, $Re = 374$) compared to the hot water ($v = 0{,}603$ m s^{-1}, $Re = 2833$), yielding a heat capacity ratio $C_r = 0{,}13$.
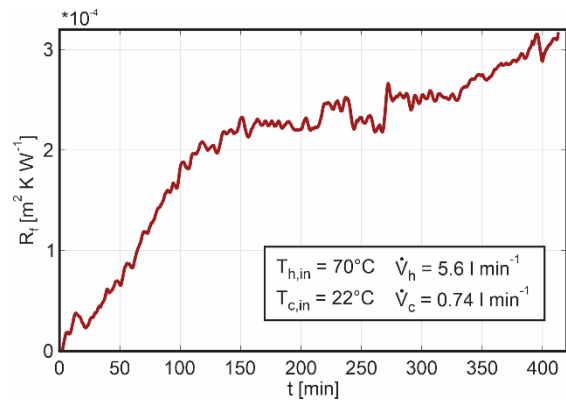

Figure 2. Fouling resistance evolution of the BPHE operating at constant conditions.

Scaling (of mainly calcite) started immediately after the foulant solution was introduced, similar to observations by Blöchl and Müller-Steinhagen [10] with particulate fouling of small aluminium oxide particles, who reported no induction period. In our experiment, this can be attributed to the absence of a fluid filter, and consequently the presence of minute particles in the aqueous salt solution, which was previously shown to considerably shorten the induction period and increase fouling rates [11]. As such, it can be said that the fouling layer growth was a result of both surface crystallization and particulate crystal deposition. Only a very short roughness–delay time of less than 5 minutes was observed, likely due to the same reasons [12], as well as because the dimple plate geometry (and roughness resulting from manufacturing) already served to increase local turbulence, meaning that only a small influence of deposit roughness on improving heat transfer can be assumed. Like many previous observations [12–14], the swift linear-like early performance degradation was followed by a gradual slow–down of fouling, directly linked to the balance between mass deposition and mass removal inside the BPHE. Mass deposition rate of calcium carbonate, often modelled as chemical–reaction controlled and of the second order [15], depends on the surface temperature-dependant supersaturation and reaction rate constant [16]. With the progression of deposition (and depletion of the solution) both influences gradually decrease, causing a reduction of fouling mass deposition rate. On the other hand, mass removal rate is increasing due to increasing wall shear stress, as well as the temperature stress in

the layer while it grows thicker [17]. Net fouling rate, the difference between deposition and removal rates, thus follows a decreasing trend.

Infrared thermography – fouling run

Infrared recordings made every 15 minutes during the above-described fouling run exposed a clearly changing temperature map of the upper flow channel because of crystallization. Initially, the set low flow rate causes the cold solution to strongly favour the flow path directly between the inlet and outlet (right side of Figure 3a). The temperature map nonuniformity points toward flow maldistribution, indicating that the upper left side of the BPHE, being a low flow velocity zone, does not contribute to solution heating. However, even at such low flow rate that induces severe maldistribution, the superb thermal performance of the dimple patterned plates can be gauged by the short length needed for the solution to reach its high outlet temperature of 65°C.
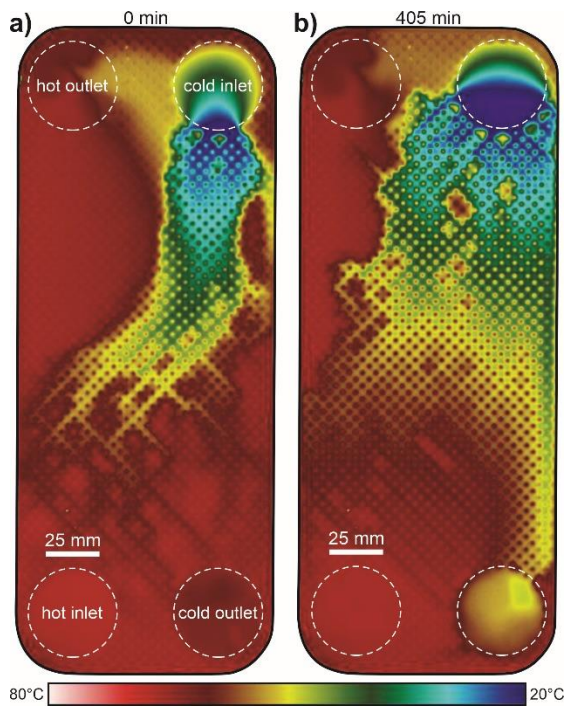

Figure 3. Temperature map at **a)** the beginning and **b)** the end of the fouling run.

Especially within the colder area of the plate, one can notice an equidistant pattern of hot spots, exhibiting higher temperatures (upwards of 10°C) than the surrounding fluid (Figure 4). These are brazing contacts, directly heated by the hot water flowing underneath, acting as flow obstructions within the channel geometry and promoting mixing. At the end of the fouling run, the outlet solution temperature was significantly lower at 58°C, with the map in Figure 3b exhibiting a larger cold area. Interestingly, the new shape of the low temperature zone indicated flow redistribution, likely due to deposit flow obstruction. Thus, the upper left side stagnation zone became smaller, indicating that the

inlet distribution of water is more homogenous. One could also observe a wedge-shaped formation at the right edge of the channel resulting in a vortex-indicative shape at the cold outlet. Even though the channel underwent favourable inlet-side re-distribution of flow, the deposit-induced increase in thermal resistance was the predominant influence on performance. Overall, the temperature distributions displayed an increased value scatter, denoting a more uniform heating, and a constantly declining mean plate temperature. To distinguish between flow stagnation areas and fouling-induced channel blockage, both manifesting as high temperature zones within the temperature map, we additionally conducted experiments with high flow rates.

Spatial characterization of fouling

To avoid maldistribution at low flow rates, which makes local characterization challenging, the BPHE upper plate temperature distribution was recorded for distinct steady states before and after the above-described fouling run, now employing higher flow rates in the cold section. At the highest employed flow rate of 3 L min^{-1} ($v = 0,323$ m s^{-1}, *Re* = 1518), this produced a homogenous temperature map of a clean BPHE, without flow stagnation zones, which is indicative of practical operation of the tested unit. Any changes to said temperature map could therefore be ascribed to fouling. To obtain an accurate pixelwise comparison with sub-millimetre resolution, the 'before' and 'after' (denoting 'clean' and 'fouled') temperature maps were first processed with an in-house developed MATLAB image processing routine. First, edge detection was used to crop-out the BPHE from the rest of each image. Then, rotation to align its longest edge in the horizontal direction and bad-pixel correction were applied. Subsequently, Circular Hough Transform (CHT)-based algorithm was used to detect the circular inlet and outlet positions within each image. Based on the detected cold inlets and outlets, a mask enclosing the cold solution area was created. To remove the influence of hot spots within this area, a point-grid local-minimum search was employed in positions between the hot spots. The cold spot pixel temperatures (Figure 4) are most indicative of the cold fluid temperature due to small influence of heat conduction through the plate from the hot spots.
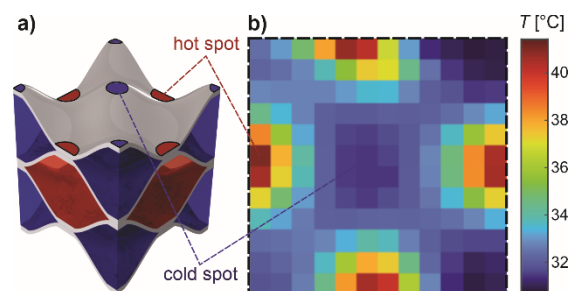

Figure 4. Graphical representation of hot and cold spots in **a)** BHPE unitary cell and **b)** in the IR image.

A grid surface was fit onto the obtained points with biharmonic interpolation to preserve its spatial features. The final step involved offsetting heat conduction through the upper plate as well as considering radiative and convective losses to the environment, to obtain the cold water temperature map of the upper channel. For the considered case of hot and cold inlet temperatures of 40°C and 22°C at flow rates of 5,6 L min^{-1} (v = 0,603 m s^{-1}, Re = 2833) and 3 L min^{-1} (v = 0,323 m s^{-1}, Re = 1518), respectively, the results are shown by Figure 5.
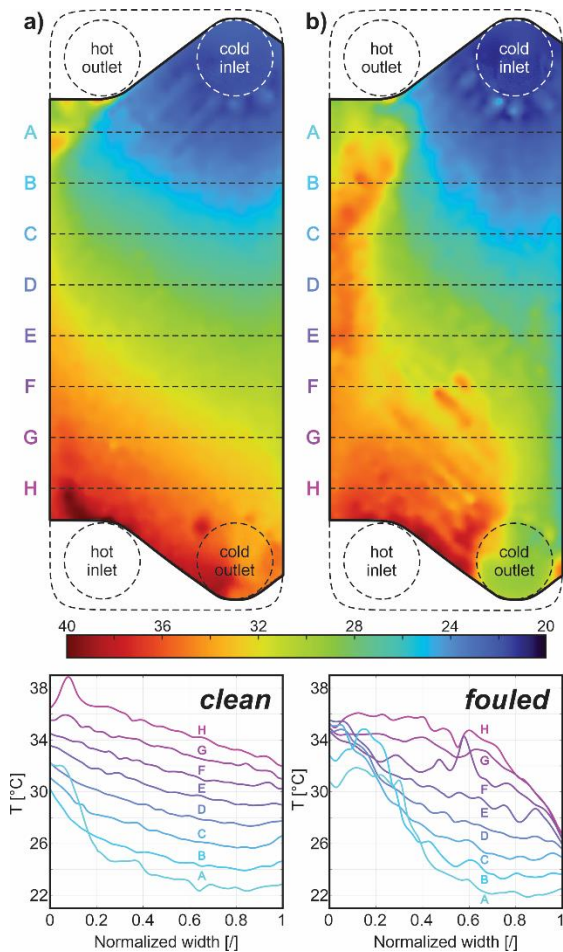

Figure 5. Extracted temperature map of the cold solution in **a)** clean state and in **b)** fouled state of the BPHE with associated temperature cross sections.

Notice the continuous shape of the temperature map of the clean BPHE (Figure 5a), originating from the dimple plate channels and inlet flow distributors. Apart from two small flow stagnation zones at the left channel edges (cross sections A and H), the isotherms are homogenously propagating from inlet to outlet of the channel. Instead, when the BPHE becomes fouled (Figure 5b), the distribution shows a high degree of skewness, especially towards the upper left side at the hot outlet. As a result of fouling, the cold outlet temperature of 35°C decreased to 28°C, corresponding to a fouling resistance of 2,45 ·10^{-4} m^2 K W^{-1}. Once the clean and fouled temperature maps were readily available, we

conducted a pixel-wise comparison to determine the local changes, depicted by Figure 6. Most of the water within the channel exhibited a temperature decrease of a few degrees, which added up to a maximum reduction of -9,2°C at the outlet. However, contrary to one's initial expectations when studying channel fouling, we show that the latter also induces a local temperature rise, in our case as high as 8,4°C. This occurred near the flow stagnation zone in the cold channel, close to the hot outlet. The temperature gradient therein is largest while the flow shear stress is low, making this area very suitable for crystallization of a sparingly soluble salt such as the one used in this study. The magnitude of the local temperature increase was far outside the increase of hot water temperature (up to 2,5°C) flowing underneath the observed channel.
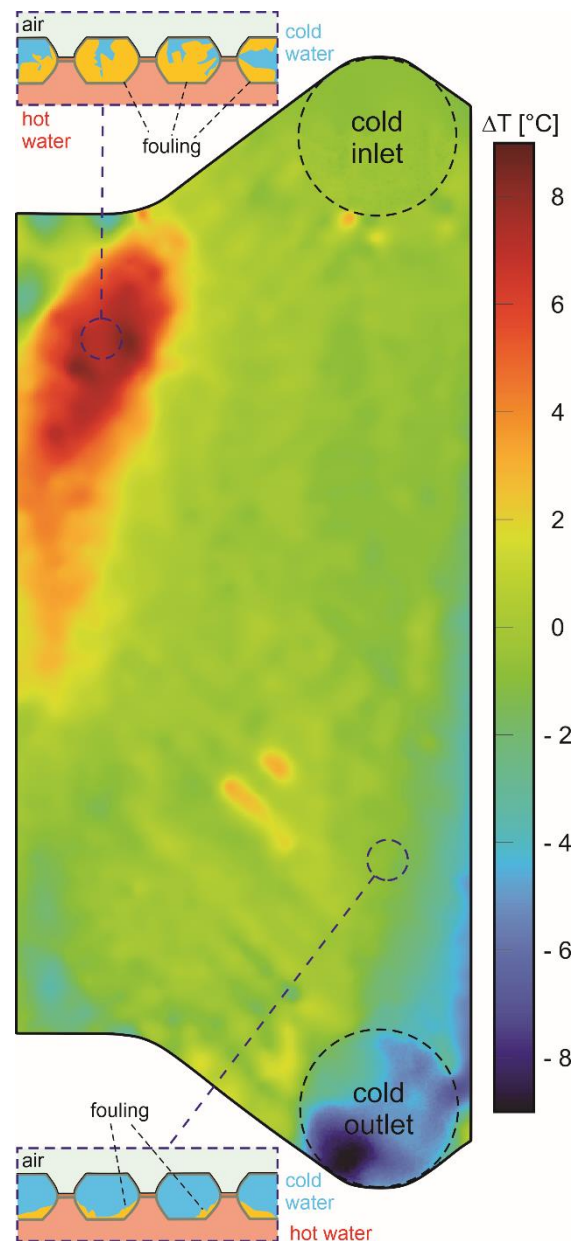

Figure 6. Crystallization fouling-induced changes to the cold water temperature map.
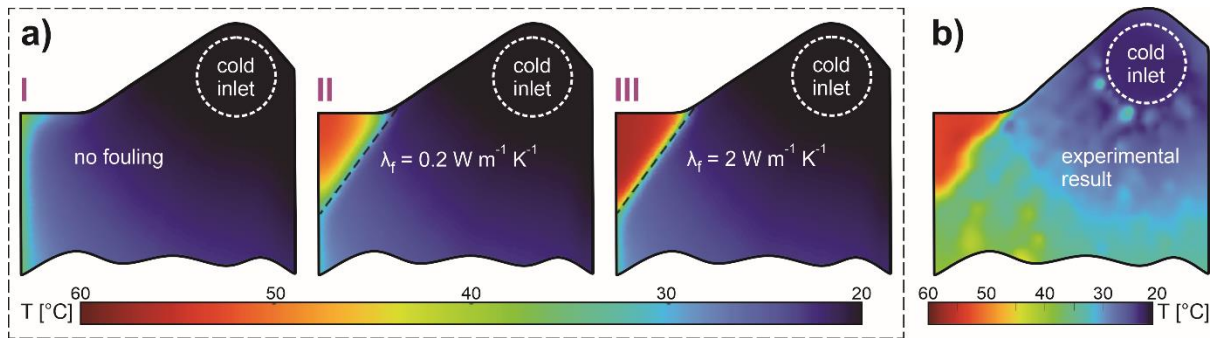
Figure 7. Outer plate temperature near the upper-left flow stagnation area, attributed to severe scale build-up, obtained with **a)** CFD simulation with different deposit properties and compared to **b)** experimental results. Black dashed lines in parts **a)** II and **a)** III correspond to solid deposit domain under the plate.

Hence, we hypothesized that severe scale build-up, covering most of the channel height, occurred therein. This assumption was verified by a computational fluid dynamics (CFD) simulation of the whole BPHE unit and comparing the area of interest with experimental results at the same inlet conditions - hot inlet temperature of 60°C with flow rate of 5,6 L min^{-1} (v = 0,603 m s^{-1}, Re = 2833) and cold inlet temperature of 20°C with flow rate of 1,9 L min^{-1} (v = 0,205 m s^{-1}, Re = 961). Shear Stress Transport (SST) turbulence model with automatic wall functions in Ansys CFX was used in the simulation. Because of computational limitations, the channel was modelled with a smooth rectangular cross section for three distinct cases. First, a clean HE was simulated to confirm that only flow stagnation cannot be the reason for such a high temperature increase of the plate (Figure 7 a-I). Subsequently, we modelled a solid domain in the corner with two drastically different thermal conductivity values in this location (Figure 7 a-II, III). The CFD solution confirmed our hypothesis that the observed high temperature increase in Figure 6 was indeed the result of heat conduction through the solid deposit underneath the plate, which can be non-intrusively measured by infrared thermography, even in complex fluid geometry. However, it also posed a challenge for future work. The temperature footprint on the upper plate, resulting from conduction through the deposit bellow, is highly dependent on deposit properties, namely its thermal conductivity. While one can confidently identify locations with severe scale build-up, its size and shape are currently subject to large uncertainty due to unknown deposit thermal conductivity, connected also to unknown porosity and the content of water within the structure.

We aim to address this challenge in our future work by coupling experimental results with CFD simulations on actual channel geometry, hopefully to obtain a trustworthy location and geometry of the deposit. Such results should also significantly improve our understanding of fouling-induced flow re-distribution and contribute to better mitigation of scaling problems in heat transfer equipment.

CONCLUSION

Experimental real-time measurements of flow rates and temperatures in a dimple BPHE was coupled with infrared thermography recordings of upper plate temperature. The latter non-intrusive method illustrated the spatiotemporal changes of the BPHE temperature map, where the degraded heat transfer characteristics manifested in a cold water temperature distribution with a lower mean but higher scatter. Interestingly, fouling also introduced a local increase of temperature in areas with severe scale build-up, where thermal conduction through the deposit caused a large local hot spot. In the analyzed case, this hot spot appeared near the hot water outlet in the low flow velocity area. As a result, the temperature map became highly skewed when compared to the one observed for a clean BPHE, indicating that a re-distribution of flow occurred as a result of local channel blockage. The comparison of experimental results and a simplified CFD model raised the challenge regarding the unknown thermal conductivity of the deposit when trying to determine its actual size and shape, which is to be addressed in the future to obtain an accurate insight into the spatiotemporal evolution of scale build-up inside a compact BPHE. Moreover, future studies should address fouling rates, unlike sped-up laboratory tests, more indicative of actual fouling problem, where the temperature changes might be different.

NOMENCLATURE

A	Heat exchange area, m^2
c_p	Specific heat capacity, J kg^{-1} K^{-1}
C_r	Heat capacity ratio
$LMTD$	Log. mean temperature difference, °C
$\dot{m}$	Mass flow rate, kg s^{-1}
$\dot{Q}$	Heat flow rate, W
Re	Reynolds number
R_f	Fouling resistance, m^2 K^1 W^{-1}
T	Temperature, °C
U	Overall heat transfer coefficient, W m^{-2} K^{-1}
v	Flow velocity, m s^{-1}
$\dot{V}$	Volumetric flow rate, L min^{-1}

Greek symbols

ΔT Temperature difference, °C

λ_f Deposit thermal conductivity, W m^{-1} K^{-1}

Abbreviations

ABS   acrylonitrile butadiene styrene
BPHE   brazed plate heat exchanger
CFD   computational fluid dynamics
CHT   circular Hough transform
DI   de-ionized
HE   heat exchanger
IR   infrared
PHE   plate heat exchanger
SST   shear stress transport

Subscripts

c   cold
f   fouling
h   hot
in   inlet
out   outlet
t   current (at time t)
0   initial (at time 0)

REFERENCES

[1] J. Berce, M. Zupančič, M. Može, I. Golobič, *A review of crystallization fouling in heat exchangers*, Processes. 9 (2021).

[2] T. Kho, H.U. Zettler, H. Müller-Steinhagen, D. Hughes, *Effect of flow distribution on scale formation in plate and frame heat exchangers*, Chem. Eng. Res. Des. 75 (1997) 635–640.

[3] T. Kho, H. Müller-Steinhagen, *An experimental and numerical investigation of heat transfer fouling and fluid flow in flat plate heat exchangers*, Chem. Eng. Res. Des. 77 (1999) 124–130.

[4] S. Freund, S. Kabelac, *Investigation of local heat transfer coefficients in plate heat exchangers with temperature oscillation IR thermography and CFD*, Int. J. Heat Mass Transf. 53 (2010) 3764–3781.

[5] K. Sarraf, S. Launay, G. El Achkar, L. Tadrist, *Local vs global heat transfer and flow analysis of hydrocarbon complete condensation in plate heat exchanger based on infrared thermography*, Int. J. Heat Mass Transf. 90 (2015) 878–893.

[6] R.L. Amalfi, J.R. Thome, *High resolution infrared measurements of single-phase flow of R245fa and R236fa within a compact plate heat exchanger , Part 1 : Experimental setup and pressure drop results*, Appl. Therm. Eng. 101 (2016) 545–554.

[7] R.L. Amalfi, J.R. Thome, *High resolution infrared measurements of single-phase flow of R245fa and R236fa within a compact plate heat exchanger , Part 2 : Heat transfer results*, Appl. Therm. Eng. 101 (2016) 555–563.

[8] J.H. Lienhard IV, J.H. Lienhard V, *A Heat Transfer Textbook*, 5th ed., Cambridge, MA, 2019.

[9] N. Epstein, *Thinking about heat transfer fouling: A 5 × 5 matrix*, Heat Transf. Eng. 4 (1983) 43–56.

[10] R. Blöchl, H. Möller—Steinhagen, *Influence of particle size and particle/fluid combination on particulate fouling in heat exchangers*, Can. J. Chem. Eng. 68 (1990) 585–591.

[11] B. Bansal, H. Müller-Steinhagen, X.D. Chen, *Performance of plate heat exchangers during calcium sulphate fouling - investigation with an in-line filter*, Chem. Eng. Process. Process Intensif. 39 (2000) 507–519.

[12] B. Bansal, X.D. Chen, H. Muller-Steinhagen, *Effect of suspended particles on crystallization fouling in plate heat exchangers*, J. Heat Transfer. 119 (1997) 568–574..

[13] E. Lee, J. Jeon, H. Kang, Y. Kim, *Thermal resistance in corrugated plate heat exchangers under crystallization fouling of calcium sulfate (CaSO4)*, Int. J. Heat Mass Transf. 78 (2014) 908–916.

[14] K.S. Song, J. Lim, S. Yun, D. Kim, Y. Kim, *Composite fouling characteristics of CaCO3 and CaSO4 in plate heat exchangers at various operating and geometric conditions*, Int. J. Heat Mass Transf. 136 (2019) 555–562.

[15] T.M. Pääkkönen, M. Riihimäki, C.J. Simonson, E. Muurinen, R.L. Keiski, *Modeling CaCO3 crystallization fouling on a heat exchanger surface - Definition of fouling layer properties and model parameters*, Int. J. Heat Mass Transf. 83 (2015) 84–98.

[16] B. Bansal, X.D. Chen, H. Müller-Steinhagen, *Analysis of "classical" deposition rate law for crystallisation fouling*, Chem. Eng. Process. Process Intensif. 47 (2008) 1201–1210.

[17] F. Brahim, W. Augustin, M. Bohnet, *Numerical simulation of the fouling process*, Int. J. Therm. Sci. 42 (2003) 323–334.